Journal of Materials Chemistry A



PAPER

View Article Online
View Journal | View Issue



Cite this: J. Mater. Chem. A, 2021, 9, 11442

Precision grain boundary engineering in commercial Bi₂Te_{2.7}Se_{0.3} thermoelectric materials towards high performance†

Shuankui Li,^a Zhongyuan Huang,^a Rui Wang,^a Chaoqi Wang,^a Wenguang Zhao,^a Ni Yang,^a Fusheng Liu,^b Jun Luo, [©] Yinguo Xiao*^a and Feng Pan [©] *^a

The strong interrelation between electrical and thermo parameters has been regarded as one of the biggest bottlenecks to obtain high-performance thermoelectric materials. Therefore, to explore a general strategy to fully decouple thermoelectric parameters and synergistically optimize the thermoelectric performance is the ultimate goal of the research on thermoelectric materials. Herein, we present a grain boundary engineering approach based on the atomic layer deposition technology to enhance the performance of commercial Bi₂Te_{2.7}Se_{0.3} thermoelectric materials. Four groups of samples, including ZnO@BTS, TiO₂@BTS, ZnO@TiO₂@BTS, and multiple-(TiO₂/ZnO)@BTS are prepared by precise controlling of the structure and composition of grain boundaries. Benefiting from the optimization of the microstructure and component of grain boundaries, the trade-off between the Seebeck coefficient, electrical conductivity and thermal conductivity is broken, resulting in a greatly enhanced thermoelectric performance. The maximum *ZT* value of 1.01 is achieved, which is 40% higher than that of a commercial Bi₂Te_{2.7}Se_{0.3} matrix. The study is promising in terms of the mass production of nanostructured thermoelectric materials with considerable improvements in performance *via* an industry compatible and reproducible route.

Received 3rd February 2021 Accepted 24th March 2021

DOI: 10.1039/d1ta01016f

rsc.li/materials-a

China

Introduction

Thermoelectric materials capable of harvesting electricity directly from waste heat are drawing growing research interest currently. The performance of a thermoelectric material is evaluated by the dimensionless figure of merit $ZT = S^2 \sigma T/\kappa$, where σ , S, κ and T are the electrical conductivity, Seebeck coefficient, thermal conductivity and absolute temperature, respectively. An excellent thermoelectric material should possess a high power factor (PF) and low thermal conductivity simultaneously, which has been proven to be extremely difficult due to the strong interdependence of thermoelectric parameters. Thus far, grain boundary engineering has been proved to be an effective route for synergistic optimization of electrical and thermal transport to substantially improve the performance of thermoelectric materials, which is based on the core concepts of thermoelectrics, including energy filtering to

balance the electrical transport and thermopower, as well as phonon scattering to reduce the lattice thermal transport performance.⁵⁻⁷ However, to achieve the decoupling of interrelated parameters by grain boundary engineering, it must be able to design, control and optimize the microstructure and component of grain boundaries at the atomic scale, which is difficult to achieve by traditional methods.

As one of the emergent and effective strategies, our recently developed atomic layer deposition (ALD) based grain boundary modification approach has shown unprecedented achievements in enhancing the performance of various thermoelectric materials, such as Bi₂Te₃-based alloys, 8,9 ZrNiSn etc. 10 To maximize the effect of grain boundary engineering, careful attention should be paid to design and regulate the microstructure and component of grain boundaries, which is crucial to decouple the interrelated thermoelectric parameters. Due to the distinctly different mean free paths of carriers and phonons, it is highly possible to simultaneously increase the Seebeck coefficient and reduce the lattice thermal conductivity with little deterioration of the carrier mobility, and finally obtain a large net enhancement of ZT by grain boundary engineering.11-13 The ALD-based grain boundary modification strategy as an ideal method to meet this challenge has been demonstrated; further study is still needed to systematically identify the grain boundary related carrier/phonon transport behaviors. 44,15 Moreover, it is of great significance to apply the strategy in fabricating

[&]quot;School of Advanced Materials, Peking University Shenzhen Graduate School, Shenzhen, 518055, China. E-mail: y.xiao@pku.edu.cn; panfeng@pkusz.edu.cn

Bhenzhen Key Laboratory of Special Functional Materials, College of Materials Science and Engineering, Shenzhen University, Shenzhen, 518060, China

School of Materials Science and Engineering, Shanghai University, Shanghai, 200444,

[†] Electronic supplementary information (ESI) available. See DOI: 10.1039/d1ta01016f

commercial thermoelectric materials with high performance, which is crucial to achieve widespread commercialization of thermoelectric technology.16

Herein, we employ ALD-based grain boundary engineering to optimize the thermal and electrical transport properties of the commercial Bi₂Te_{2,7}Se_{0,3} (BTS) thermoelectric material (Fig. 1). To investigate the effects of the microstructure and component of grain boundaries, four groups of samples, including ZnO@BTS, TiO2@BTS, ZnO@TiO2@BTS, and multiple-(TiO2/ ZnO)@BTS with designed grain boundaries are prepared.

The ZnO@BTS and TiO2@BTS samples with different thicknesses of corresponding ALD coating layers are labeled as BZ, and BT, respectively. The ZnO@TiO2@BTS samples, in which the BTS matrix is coated with 15 ALD TiO₂ layers firstly, and then coated with different thicknesses of ZnO layers are denoted as BTZ. The multiple-(TiO2/ZnO)@BTS samples with a total 20 ALD cycles and multilayer alternating structure are labeled as M-BTZ. The experimental results show that by tailoring the microstructure at the atomic scale, the interrelation between the Seebeck coefficient, electrical conductivity and thermal conductivity can be untangled, and simultaneously modification of all thermoelectric parameters toward the desired direction is achieved. Typically, the PF can be enhanced by approximately 5–10% and κ_{latt} can be reduced by more than 30%, resulting in great enhancement in ZT values. As shown in Fig. 1b, for the BZ-20 sample with ZnO/BTS heterogeneous grain boundaries, the maximum ZT value of 0.95 is achieved, which is

25% higher than that of the commercial BTS thermoelectric material. Significantly, the thermoelectric performance could be further enhanced by introducing multiple-ALD coatings (Fig. 1c), and a high ZT of about 1.01 (at 400 K) is obtained for the BTZ-15/50 sample, which is an excellent value compared with that of the reported n-type BT-based nanostructured TE materials. Our findings demonstrate that the ALD-based grain boundary engineering could be applied as a general route to decouple the strongly interrelated parameters and thus to enhance thermoelectric performance, which might also be effective for other thermoelectric materials beyond Bi₂Te₃related materials.17-20 In the present work, the commercial BTS thermoelectric material is used as the matrix material, implying the high industrial compatibility, great commercial value and enormous application potential of this strategy.21,22

Experimental section

Materials synthesis

A commercial BTS alloy rod is purchased from Wangu Electronic Materials Co., Ltd. BTS powders were obtained by ballmilling the bulk BTS alloy with zirconia balls at a milling speed of 800 rpm for 60 min in ambient Ar.

Coating the BTS powders by ALD

ALD layers were coated on the surface of BTS powder in a homemade continuous-flow ALD reactor operated under

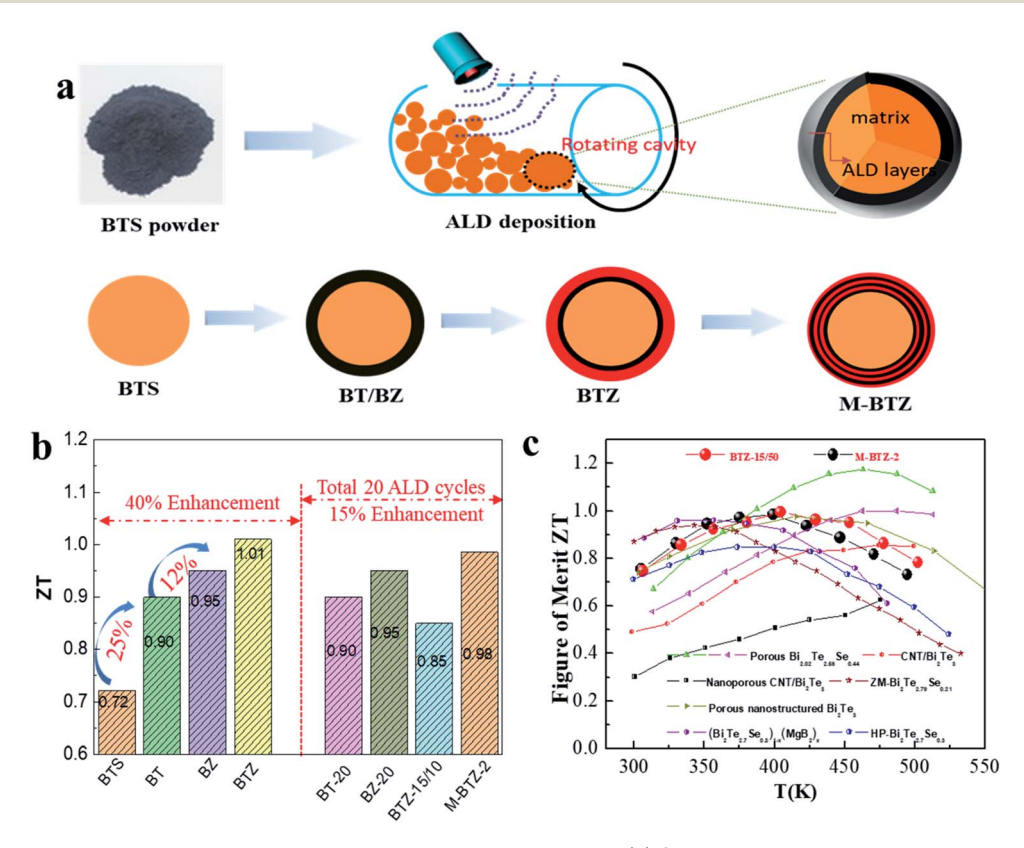


Fig. 1 (a) A schematic of the grain boundary engineering strategies based on ALD. (b) Comparison of the maximum ZT value of the samples in this work. (c) Temperature dependent ZT for the as-prepared samples, including a comparison to the available reference.

a base pressure of ~ 1 torr. Typically, the 10 g as-prepared BTS matrix is transferred into an ALD chamber equipped with a vertical stainless rotating sample chamber. TiO₂ and ZnO are deposited using tetrakisdimethylamido-titanium (TDMAT) and DEZ and H₂O as ALD precursors at 150 °C, respectively. The precursor dose and purge time were 30 seconds and 60 seconds, respectively. Ar gas served as both a carrier and a purging gas.

ZnO@BTS and TiO2@BTS with X cycles of ALD coating layer are labeled as BZ-X, and BT-X, respectively. The ZnO@TiO2@BTS samples, in which the BTS matrix was coated with 15 ALD TiO2 layers firstly, and then coated with X cycles ZnO ALD coating layers, are denoted as BTZ-15/X. Moreover, the multiple-(TiO2/ZnO)@BTS samples with a total 20 ALD cycles and multilayer alternating structure labeled M-BTZ are prepared. For example, the M-BTZ-1 sample possess the 1 cycle ZnO ALD layer/1 cycle TiO2 ALD layer alternating structure with a total 20 ALD cycles.

Characterization

X-ray powder diffraction (XRD) measurements are performed on a Bruker D8 Advance X-ray diffractometer; field-emission scanning electron microscopy (SEM) analysis of the morphology and element distribution is carried out on a Zeiss SUPRA-55 microscope integrated with an Oxford EDS; X-ray photoelectron spectra (XPS) were acquired on a Thermo Fisher ESCALAB 250X surface analysis system equipped with a monochromatized Al anode X-ray source (X-ray photoelectron spectroscopy, XPS, $h\nu=1486.6$ eV). The overall morphology and detailed crystallographic information are deduced from high-resolution field-emission transmission electron microscopy (FETEM; JEOL-3200FS, 300 kV). A focused ion beam system (FIB; JIB 4601F, JEOL) is used to prepare the TEM samples of the sintered bulk sample.

Thermoelectric measurements

The BTS powders pressed into pellets by hot pressing (HP) at 673 K for 30 min under vacuum with a uniaxial pressure of 60 MPa. The pellets are cylinders with 10 mm diameter and 12 mm height. The disk with a thickness of around 2 mm was cut from the sintered pellets to measure the thermal conductivity, and a cuboid about 3 mm \times 3 mm \times 10 mm is cut to measure σ and S. The electrical conductivity and Seebeck coefficient are measured using a ULVAC ZEM-3 within the temperature range 300–500 K. The total thermal conductivity ($\kappa_{\rm tot}$) is calculated through $\kappa_{\rm tot} = DC_{\rm p}\rho$, where D, $C_{\rm p}$, and ρ are the thermal diffusivity coefficient, specific heat capacity, and density, respectively. The thermal diffusivity coefficient is measured using a laser flash apparatus using a Netzsch LFA 467 from 300 to 500 K, and the specific heat ($C_{\rm p}$) is tested using a differential scanning calorimeter (Mettler DSC1), and the density (ρ) is calculated by using the mass and dimensions of the pellet.

Results and discussion

Design of heterogeneous grain boundaries

In order to systematically investigate the effects of the microstructure and component of grain boundaries, the ALD technique is employed to design and construct heterogeneous grain

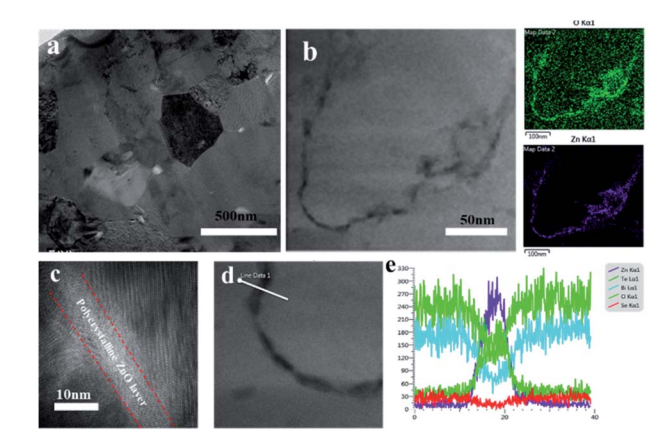


Fig. 2 The microstructure of the as-prepared BZ sample with ZnO/BTS heterogeneous grain boundaries. (a) and (b) Low magnification TEM image and corresponding EDS mapping images. (c) HRTEM images of the ZnO/BTS heterogeneous grain boundaries. (d) HRTEM images and (e) corresponding EDS line mapping at ZnO/BTS heterogeneous grain boundaries.

boundaries in the commercial BTS thermoelectric material. According to our previous studies, the growth rate of TiO2 and ZnO coatings on the BTS surface is around 0.8 Å and 1.2 Å per ALD cycle.9,14 As illustrated in Fig. 1a, the uniform ALD multilayer is introduced successfully on the surface of BTS powders (i.e., core-shell structured powders) to construct the heterogeneous grain boundaries. As demonstrated in the previous report, the ZnO interlayer can be maintained during the hot pressing process, which results in the formation of ZnO/BTS heterogeneous grain boundaries.14 The TEM analysis confirmed the presence of ZnO/BTS heterogeneous grain boundaries, as shown in Fig. 2. The low magnification TEM image (Fig. 2a) reveals that the BTS grains with an average size of about 600 nm are closely packed, which agrees well with the EBSD results. The magnified TEM image (Fig. 2b) and corresponding EDS line-scans reveal that the approximately 5-8 nm ZnO layer existed at the grain boundaries. Moreover, as shown in Fig. 2c, the ZnO layer is of amorphous state, which is consistent with the amorphous characteristic of the ALD film. It is known that the ZnO layers could lead to the precipitation of Te nanodots at the ZnO/BTS interface for the BTS matrix synthesized by a solution-based strategy.14 By contrast, in present work, the composition segregation of the BTS matrix at the ZnO/BTS heterogeneous grain boundaries is not observed, which illustrates that the BTS is stable during the hot press process. This can be attributed to the larger grain size and high chemical stability of the BTS matrix synthesized by the zone melting method. The above experimental results indicate that the ZnO/BTS heterogeneous grain boundaries could be introduced to the BTS matrix via the ALD approach.

Tailoring the microstructure by introducing multiple ALD coating

It is worth noting that the interaction mechanism between the ALD layers and BTS matrix is different for the different ALD coatings. For the BT samples, the TiO₂ layer will react with the BTS matrix and grain boundary reconstruction occurs during the sintering process.7 Consequently, oxygen impurity appears in the form of large sized Bi₂O_x and O-related dislocation clusters in the BTS matrix grain, due to the diffusion of oxygen atoms from the grain boundaries to the BTS matrix. This phenomenon is also consistent with the present results of BT samples using commercial BTS as the matrix. As shown in Fig. 3a, the sample is composed of approximately 500-800 nm BTS grains, which is similar to that of BZ samples. There are some Bi₂O_r precipitates embedded in the grain boundaries of the BTS matrix and they can also be clearly revealed in the corresponding EDX mapping image. Moreover, due to the diffusion of a small amount of oxygen into the BTS crystal lattice during the sintering process, high density O-related dislocation clusters can also be observed in the BTS grain. Fig. 3a-c show the comparison of the microstructure of the BT, BTZ and M-BTZ. Similar to the BT samples, large-scale Bi₂O_x precipitates are always observed in the BTZ and M-BTZ samples, indicating that the multiple-ALD layer could react with the BTS matrix during the sintering process. The corresponding EDS line scan profiles illustrate homogeneous elemental distribution at the grain boundaries, and no Zn rich region is detected. High density O-related dislocation clusters can also be observed on the BTS grains, which are similar to the observation in BT samples (Fig. 3e). Different from the BZ and BT samples, widespread nanopores could be observed at the grain boundaries in the BTZ and M-BTZ samples (Fig. 3b-d and S1†). In this

case, it seems that the introduced ultrathin TiO2 layer could promote the reaction between the ZnO layer and BTS matrix. For the BTZ samples, only about 1 nm TiO2 layer (15 ALD circles) is introduced to the BTS matrix surface, which can effectively give rise to the reaction between the ZnO layer and BTS matrix, and finally results in the formation of the microstructure similar to that of BT samples. As shown in Fig. 3e, a sawtooth-type grain boundary with an about 5 nm roughness is formed, and the corresponding EDS line-scan profiles illustrate evidently a homogeneous elemental distribution at the grain boundaries. Compared with the BTZ, the M-BTZ samples with multi-ALD layers possess higher density of nanopores as well as larger grain boundary roughness, as shown in Fig. 3e and S2.† Obviously, the formation of nanopores and sawtooth grain boundaries is related to the reaction between multiple ALD coatings and the BTS matrix during the sintering process, which will be discussed below.

The formation mechanism of the special microstructure

Fig. 4a presents the EBSD image taken from the pellet sample, suggesting the widely distributed grain sizes with random crystallographic orientations. The average size of the BTS grain is about 600 nm (Fig. 4b), which is in agreement with the TEM results. In order to further elucidate the composition of the asprepared bulk samples, the chemical binding states of Zn ions in BZ, BTZ, M-BTZ samples are examined via XPS as shown in Fig. 4c. The 2p core level binding energies of Zn located at

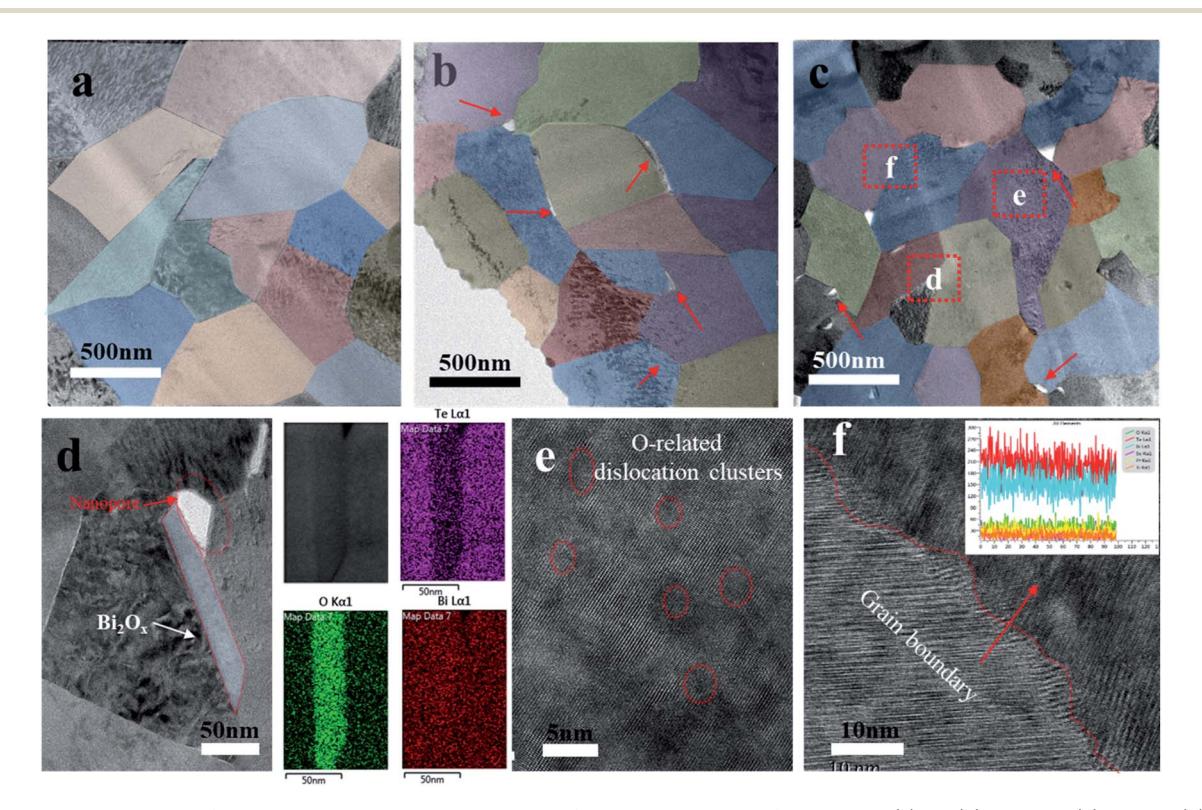


Fig. 3 TEM characterization of the as-prepared samples. Low magnification TEM image of the sample (a) BT, (b) BTZ, and (c) M-BTZ. (d) HRTEM image and corresponding EDS elemental maps of the red rectangular region in (c). The HRTEM image of (e) the O-related dislocation cluster and (f) sawtooth grain boundaries of the red rectangular region in (c).

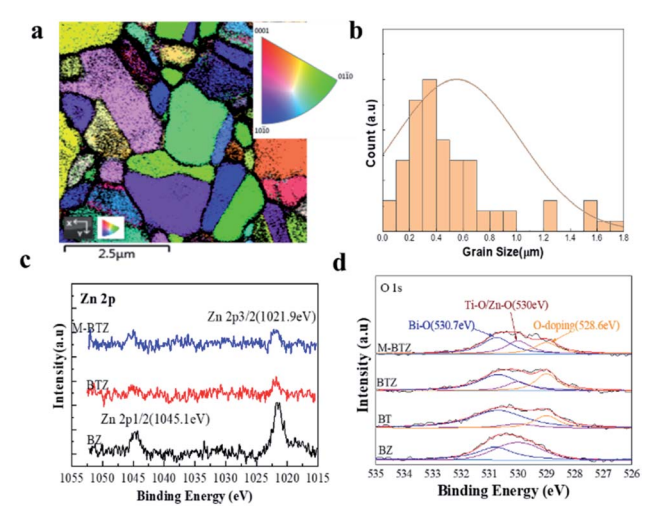


Fig. 4 (a) The EBSD maps and (b) corresponding size distribution of the BTS grains of the as-prepared sample. XPS spectra for the as-prepared ALD coated BTS sample. (c) Zn 2p peaks of the BZ, BTZ and M-BTZ samples. (d) O 1s peaks of the BZ, BT, BTZ and M-BTZ samples.

 $1044.5 \text{ eV} (2p_{1/2})$ and $1021.4 \text{ eV} (2p_{3/2})$ are clearly observed in the BZ samples. However in the BTZ and M-BTZ samples, the peaks of the Zn 2p core level almost disappeared, indicating the loss of Zn during the sintering process. Considering the low melting point and high vapor pressure of metallic Zn, it can be concluded that the evaporation of metallic Zn nanodots induced by the interfacial chemical reaction may occur during the sintering process, leading to the formation of nanopores and sawtooth grain boundaries. In the O 1s spectra (Fig. 4d), three peaks can be observed, the Zn-O/Ti-O peak at 530 eV, and the Bi-O peak at 531.6 eV as well as the peak with a lower binding energy (528.6 eV) originating from oxygen atoms of the O-related dislocation clusters in the Bi₂Te₃ matrix.⁷ For the BZ samples, the O 1s spectra can be deconvoluted into two main peaks originating from ZnO and BiOx. However, the Ti-O peak at 530 eV almost vanished and the O-doping peak at 528.6 eV emerges in the O 1s spectra of BT samples. Similar results are also obtained in the BTZ and M-BTZ samples, which further confirm the above results.

Engineering of electrical transport properties at grain boundaries

The thermoelectric properties of the as-prepared samples measured to investigate the effect of grain boundary engineering (Fig. S4†). Fig. 5a show the variation in the resistivity of the BZ, BT, BTZ samples measured at room temperature as a function of the number of ALD cycles. It is found that σ (~876.8 S cm $^{-1}$) and S ($-152.9~\mu V~K^{-1}$) of the commercial BTS sample at 300 K are comparable to those of the reported Bi $_2$ Te $_3$ -based thermoelectric material. $^{17-20}$ For the BZ samples, the electrical transport properties are significantly affected by the barriers at the ZnO/BTS interface \emph{via} the energy filtering effect. As theoretically predicted, the so-called "energy filtering" effect is related to the potential barriers (related to the momentum relaxation length λ_p and the energy relaxation length λ_e) and

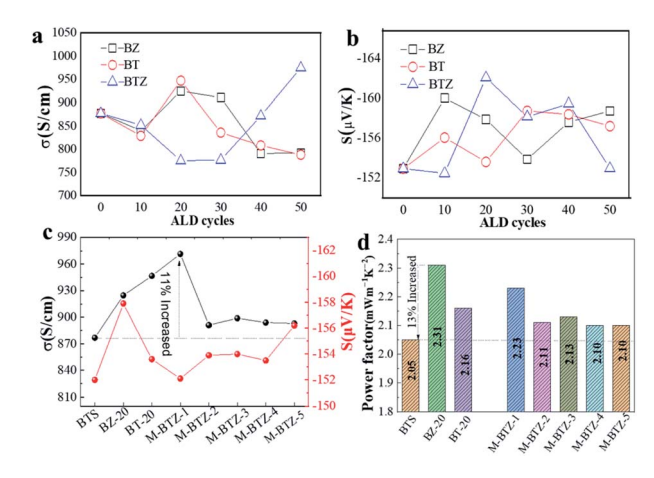


Fig. 5 Modulation of electrical properties through ALD-based grain boundary engineering. The variations in the value of (a) σ , and (b) S of the as-prepared SPS BT, and BTZ samples measured at room temperature as a function of the number of ALD cycles. (c) σ and S and (d) power factor at 300 K for the M-BTZ samples.

grain size (d). For the sample with a grain size d, the PF can be enhanced by tunning the potential barriers, depending on the relationship between grain size d, the momentum relaxation length λ_p and the energy relaxation length λ_e . Thereby, the design and control of the grain size and interface potential barrier by grain boundary engineering to satisfy the relationship $\lambda_{\rm p} < d < \lambda_{\rm e}$ the trade-off between σ and S could be broken, resulting in a net improvement in $S^2\sigma$. This scenario is consistent with our result that for samples with an appropriate ZnO thickness (BZ-20 and BZ-30), σ and S are simultaneously improved. Conversely, for the samples with a thick ZnO layer (more than 30 ALD cycles), σ decreases due to the suppression of the electron transport by the ZnO/BTS heterogeneous grain boundaries. As a result, a high PF of 2.31 mW m⁻¹ K⁻² was obtained at 300 K for BZ-20 due to the simultaneous enhancement of σ and S. As discussed above, due to the reaction between the ALD coating and the BTS matrix during the sintering process, the oxygen impurity in the BT samples appears in the form of large sized Bi2Ox and O-related dislocation clusters, which is critical to adjust their electrical transport properties. The O atoms in the samples with a thin ALD coating (below the 30 ALD cycles) mainly exist in the form of O-related dislocation clusters, which shows a positive contribution to σ and S (Fig. S5†). Typically, both σ (\sim 946 S cm⁻¹) and S (\sim 153.6 $\mu V K^{-1}$) of BT-20 increase simultaneously, which can be ascribed to the donor-like effect and the energy filtering effect of O-related dislocation clusters. These clusters in the BTS grain would lead to the generation of Te vacancies, which can donate electrons and pull the Fermi energy up to higher levels, leading to a positive contribution on the n-type conductivity. Moreover, the O-related dislocation clusters accompanied by large-scale lattice distortion in the BTS grain can be treated as charged Coulomb scattering centers, which will enhance S through the energy filtering effect. As the thickness of the ALD layer keeps increasing, the O atoms mainly exist as large-scale Bi2Ox precipitates, which is quite similar to the case of surface

oxidation. The formation of large-scale Bi₂O_x precipitates has a negative effect on both S and σ . Due to the simultaneously enhanced σ and S, the highest power factor of about 2.16 mW $m^{-1} K^{-2}$ at 300 K is obtained for the BT-20 sample.

For the BTZ and M-BTZ samples, the reaction between the ALD coating and the BTS matrix also occurred, which resulted in oxygen impurities as well as high density nanopores. The combination of the two effects makes σ first decrease with increasing numbers of ZnO ALD cycles for the BTZ samples (below 30 ALD cycles), which is obviously different from that of BT and BZ samples (Fig. S6 \dagger). Surprising, above 30 ALD cycles, σ increases with increasing numbers of ZnO ALD cycles, which may originate from small amount Zn doping in BTZ samples. Different from the Ti doping, the Zn doping in the BTS matrix could significantly increase the electrical conductivity due to the increased electron concentration.29 Owing to the simultaneously enhanced σ and S, the power factor increases, and the value for the BTZ-50 sample reaches 2.31 mW m⁻¹ K⁻² at 300 K.

In fact, our experimental results show that the trade-off between σ and S could be broken for all the samples. This suggests that ALD-based grain boundary engineering is a general route to optimize the electrical transport properties of thermoelectric materials. It is observed that for the BT and BZ samples, an appropriate ALD layer thickness (20 ALD cycles) is essential to decouple σ and S. Thus, ZnO/TiO₂ multilayers with a fixed total ALD cycles (20 cycles) and various periods are introduced to the surface of the BTS matrix, marked M-BTZ. As discussed above, the M-BTZ samples exhibit a similar microstructure feature to the BTZ samples, except for the high density nanopores and sawtooth grain boundaries. It can be found that compared with the BTS matrix, the simultaneously enhanced σ and S are obtained for all the M-BTZ samples, as shown in Fig. 5c and S7.† Due to the optimized electrical transport properties, the PF of M-BTZ samples increases by approximately 5-10% in comparison with that of the BTS matrix. Collectively, ALD-based grain boundary engineering could break the tradeoff between σ and S and thus results in a net great enhancement of PF, which highlights that this method is a feasible and promising strategy to optimize the electrical transport properties and may be applicable to other thermoelectric material systems.

Thermal transport properties

As expected, compared with the thermal conductivity (κ_{tot}) of the BTS matrix (\sim 1.094 W m⁻¹ K⁻¹ at 300 K), the κ_{tot} of all the ALD coated samples is significantly decreased. Fig. 6a shows the variation in the κ_{tot} of the BZ, BT, and BTZ samples measured at 300 K as a function of the number of ALD cycles. In general, κ_{tot} decreases with increasing number of the ALD cycles for the BZ, BT, and BTZ samples. Typically, for the BZ-20 sample with the ZnO/BTS heterogeneous grain boundary, the κ_{tot} value significantly reduces by approximately 15% although σ exceeds that of the BTS matrix. As mentioned above, the introduced ZnO/BTS heterogeneous grain boundary leads to the enhanced scattering of low-frequency phonons. Meanwhile, for the BT and BTZ samples, the introduced O-related dislocation clusters as

well as the large sized Bi_2O_x contribute to low κ_{tot} . Importantly, the κ_{tot} of the BTZ samples is much lower than those of the BZ and BT samples, which may originate from the contribution of nanopores and sawtooth grain boundaries. Typically, a low κ_{tot} of about 0.893 W m⁻¹ K⁻¹ at 300 K is obtained for the BTZ-30 sample. It is well known that κ_{tot} is the sum of the electrical $(\kappa_{\rm e})$, lattice $(\kappa_{\rm latt})$, and bipolar $(\kappa_{\rm bi})$ thermal conductivities. The Wiedemann-Franz law could be used to describe κ_e , expressed by $\kappa_e = L\sigma T$, where L is the Lorenz number $(L = 1.5 + \exp(-|S|/$ 116)). Thus, by subtracting κ_e from κ_{tot} , the $\kappa_{latt} + \kappa_{bi}$ value could be obtained. It is noted that in the low temperature region (T < 350 K), the contribution of $\kappa_{\rm bi}$ could be ignored, and $\kappa_{\rm latt}$ could be obtained by subtracting κ_e from κ_{tot} . As shown in Fig. 6b, the $\kappa_{\rm latt}$ of the BTS matrix is about 0.62 W m⁻¹ K⁻¹ at 300 K, which is comparable to that of the previously reported results.30,31 By grain boundary engineering, κ_{latt} can be effectively suppressed. Typically, for the BZ-20 sample, the κ_{latt} value is about 0.44 W m⁻¹ K⁻¹ at 300 K, reduced by approximately 30% compared with that of the BTS matrix. The BT-20 sample with O-related dislocation clusters and Bi_2O_x nanoprecipitates shows a κ_{latt} value of about 0.46 W m⁻¹ K⁻¹ at 300 K. It is generally assumed that the grain boundary scatters the long-wavelength phonons and the dislocations scatter the mid-wavelength phonons. For the BTZ samples containing O-related dislocation clusters, Bi₂O_r nanoprecipitates, nanopores and sawtooth grain boundaries, κ_{latt} is further reduced, the minimum value of 0.394 W m⁻¹ K⁻¹ at 300 K obtained for BTZ-15/50. Moreover, by tailoring the microstructure at the atomic scale, the value of κ_{latt} could be minimized; a minimum value of 0.386 W m⁻¹ K⁻¹ at 300 K is obtained for M-BTZ-1, reduced by approximately 10% and 15% compared with that of BZ-20 (0.44 W m⁻¹ K⁻¹) and BT-20 $(0.46 \text{ W m}^{-1} \text{ K}^{-1})$, respectively. Considering the same ALD cycles of the three samples, the tremendous reduction of κ_{latt} can be ascribed to the enhanced phonon scattering at the sawtooth grain boundary with nanoscale roughness. Via ALDbased grain boundary engineering, the scattering centers with different scales are introduced in the sample to achieve full wavelength phonon scattering.

It is known that the interfacial thermal resistance can be calculated to estimate the effect of the microstructure and component of the grain boundary.32 In this model the interfacial thermal resistance contains contributions from the initial BTS matrix and an additional contribution from the heterogeneous grain boundary.³³ Then, the κ_{latt} of the as-prepared sample is fitted to $\kappa_{\text{latt}}^{-1} = \kappa_{\text{BTS}}^{-1} + R_{\text{K}}/d_{\text{eff}}$, where d_{eff} is the average grain size, which is about 0.6 µm determined by the EBSD and TEM results; $R_{\rm K}$ is the additional interfacial thermal resistance (for a unit area), reflecting the grain boundary contribution for the reduction of κ_{latt} . The κ_{latt} of M-BTZ-1 is calculated to confirm the effectiveness of the model, as shown in the inset of Fig. 5d. It is found that the results agree well with the experimental values, excepting that the value of κ_{latt} is slightly lower than the calculated curve in a high temperature range due to the contribution of bipolar diffusion. $R_{\rm K}$ at 300 K of the as-prepared samples is calculated through the model with $d_{\rm eff} = 0.6 \mu m$, as shown in Fig. 6d. It is clearly observed that compared with the values of the BZ and BT samples, the $R_{\rm K}$

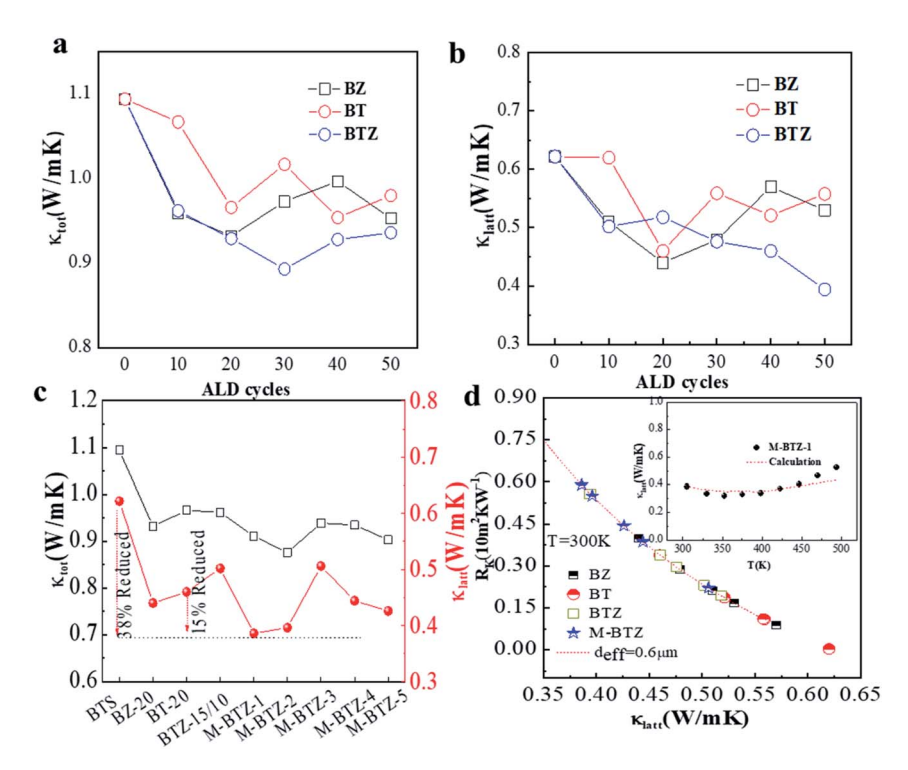


Fig. 6 Modulation of thermal transport properties through ALD-based grain boundary engineering. The variations in the value of (a) κ_{tot} and (b) κ_{latt} of the as-prepared BT, and BTZ samples measured at room temperature as a function of the number of ALD cycles. (c) κ_{tot} and κ_{latt} at 300 K for the M-BTZ samples. (d) Room temperature κ_{latt} and calculated R_{K} of the as-prepared BT and BTZ samples (the inset shows the κ_{latt} of M-BTZ-1 compared with the calculated results).

values of the BTZ and M-BTZ samples are increased, which can be ascribed to the enhanced phonon scattering at designed grain boundaries.

The present work clearly demonstrates that through ALD-based grain boundary engineering, the decoupling of the thermoelectric parameters could be achieved. As shown in Fig. 7a, for the asprepared BZ, BT, BTZ and M-BTZ samples, the substantially enhanced PF and suppressed $\kappa_{\rm latt}$ are obtained. Typical, for the BZ-20 sample, the enhanced PF and simultaneously reduced $\kappa_{\rm latt}$ lead to a relatively high $ZT\sim0.95$ at 400 K, which is $\sim\!32\%$ higher than that of pristine BTS. This result is also consistent with our previous work using BTS nanoparticles as the matrix. Moreover, the slightly

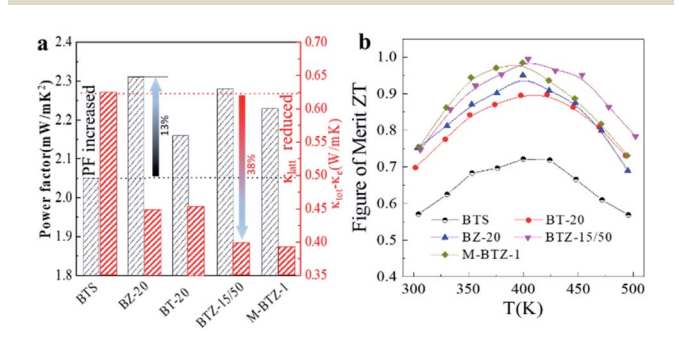


Fig. 7 Typical value of the (a) power factor and κ_{latt} of the as-prepared BZ, BT, BTZ, and M-BTZ samples measured at room temperature compared with those of the BTS matrix. (b) Thermoelectric figure of merit ZT of the typical samples.

improved PF (5.4%) and significantly reduced κ_{latt} (26%) promise a large enhancement (20%) in the ZT value of the BT-20 sample. Furthermore, by tailoring the microstructure in the atomic scale through introducing multiple ALD coatings, κ_{latt} could be further reduced. Consequently, a minimum value of 0.394 W m^{-1} K⁻¹ at 300 K is obtained for BTZ-15/50, which decreases by approximately 38% and 15% compared to those of the BTS matrix and BT-20, respectively. As a result, the maximum ZT value of 1.01 is achieved, which is 40% higher than that of a commercial BTS thermoelectric material Fig. 7b and S8.† shows the comparison with other n-type BT-based nanostructured TE materials; it is an excellent and highly competitive value near the room temperature range. Thereby, the study demonstrates that ALD-based grain boundary engineering could be a general route to decouple the strongly interrelated parameters for significantly enhanced thermoelectric performance, which is effective for the other thermoelectric materials beyond Bi₂Te₃-related materials.¹⁰ Specifically, in the present work the commercial BTS thermoelectric material is used as the matrix material, implying the high industrial compatibility, great commercial value and enormous application potential of this strategy. Thus, the present work provides insight into the structural design and synthesis of broadly functional hybrid thermoelectric material systems.

Conclusions

In summary, ALD-based grain boundary engineering has been employed to improve the performance of a commercial BTS thermoelectric material by decoupling and optimizing thermoelectric parameters. The experimental results show that by tailoring the microstructure at the atomic scale, the trade-off between the Seebeck coefficient, electrical conductivity and thermal conductivity is broken, and simultaneously modification of all parameters toward the desired direction can be achieved. For the as-prepared BZ, BT, BTZ and M-BTZ samples, the substantially enhanced PF and suppressed κ_{latt} are obtained. Typically, the PF increases by approximately 5-10% and κ_{latt} reduces above 30%, promising the net great enhancement of ZT values. As a result, the optimized sample presents an outstanding performance, with high ZT reaching 1.01 (at 400 K), which is about 40% larger than that of a commercial BTS matrix. The study shows that ALD-based grain boundary engineering could be a general route to decouple the strongly interrelated parameters for significantly enhanced thermoelectric performance, which is effective for other thermoelectric materials beyond Bi₂Te₃-related materials.

Conflicts of interest

There are no conflicts to declare.

Acknowledgements

The work was financially supported by the National Natural Science Foundation of China (No. 21905007), and Guangdong Basic and **Applied Basic** Research Foundation (2019A1515010832).

Notes and references

- 1 J. Mao, G. Chen and Z. F. Ren, Nat. Mater., 2020, 1-8.
- 2 B. Poudel, Q. Hao, Y. Ma, Y. C. Lan, A. Minnich, B. Yu, X. Yan, D. Z. Wang, A. Muto, D. Vashaee, X. Y. Chen, J. M. Liu, M. S. Dresselhaus, G. Chen and Z. F. Ren, Science, 2008, **320**, 634-638.
- 3 C. Xiao, Z. Li, K. Li, P. Huang and Y. Xie, Acc. Chem. Res., 2014, 47, 1287-1295.
- 4 W. G. Zeier, A. Zevalkink, Z. M. Gibbs, G. Hautier, M. G. Kanatzidis and G. J. Snyder, Angew. Chem., Int. Ed., 2016, 55, 2-18.
- 5 H.-S. Kim, S. D. Kang, Y. Tang, R. Hanus and G. J. Snyder, Mater. Horiz., 2016, 3, 234-240.
- 6 J. Mao, Y. Wang, Z. Liu, B. Ge and Z. Ren, Nano Energy, 2017, 32, 174-179.
- 7 J.-H. Bahk and A. Shakouri, Appl. Phys. Lett., 2014, 105, 052106.
- 8 S. Li, W. Zhu, Y.-G. Xiao and P. Feng, Chin. J. Struct. Chem., 2020, 39, 831-837.
- 9 S. Li, M. Chu, W. Zhu, R. Wang, Q. Wang, F. Liu, M. Gu, Y. Xiao and F. Pan, Nanoscale, 2020, 12, 1580-1588.
- 10 Y. Zhang, S. Li, F. Liu, C. Zhang, L. Hu, W. Ao, Y. Li, J. Li, H. Xie, Y. Xiao and F. Pan, J. Mater. Chem. A, 2019, 7, 26053-26061.

- 11 Y. Lin, M. Wood, K. Imasato, J. J. Kuo, D. Lam, N. Mortazavi, T. J. Slade, S. A. Hodge, K. Xi, M. G. Kanatzidis, D. R. Clarke, M. C. Hersam and G. J. Snyder, Energy Environ. Sci., 2020, 13, 4114-4121.
- 12 A. M. Dehkordi, S. Bhattacharya, T. Darroudi, J. W. Graff, U. Schwingenschlögl, H. N. Alshareef and T. M. Tritt, Chem. Mater., 2014, 26, 2478-2485.
- 13 D. Wu, Y. Pei, Z. Wang, H. Wu, L. Huang, L. Zhao and J. He, Adv. Funct. Mater., 2014, 24(48), 7763-7771.
- 14 S. Li, Y. Liu, F. Liu, D. He, J. He, J. Luo, Y. Xiao and F. Pan, Nano Energy, 2018, 49, 257-266.
- 15 S. Li, X. Liu, Y. Liu, F. Liu, J. Luo and F. Pan, Nano Energy, 2017, 39, 297-305.
- 16 K.-C. Kim, S.-S. Lim, S. H. Lee, J. Hong, D.-Y. Cho, A. Y. Mohamed, C. M. Koo, S.-H. Baek, J.-S. Kim and S. K. Kim, ACS Nano, 2019, 13(6), 7146-7154.
- 17 B. Xu, T. Feng, M. T. Agne, L. Zhou, X. Ruan, G. J. Snyder and Y. Wu, Angew. Chem., Int. Ed., 2017, 56, 1-7.
- 18 Q. Zhang, L. Xu, Z. Zhou, L. Wang, W. Jiang and L. Chen, J. Appl. Phys., 2017, 121(5), 055104.
- 19 K. T. Kim, S. Y. Choi, E. H. Shin, K. S. Moon, H. Y. Koo, G.-G. Lee and G. H. Ha, Carbon, 2013, 52, 541-549.
- 20 Y. Wang, W. Liu, H. Gao, L.-J. Wang, M. Li, X.-L. Shi, M. Hong, H. Wang, J. Zou and Z.-G. Chen, ACS Appl. Mater. Interfaces, 2019, 11(34), 31237-31244.
- 21 B. Chen, J. Li, M. Wu, L. Hu, F. Liu, W. Ao, Y. Li, H. Xie and C. Zhang, ACS Appl. Mater. Interfaces, 2019, 11(49), 45746-45754.
- 22 L. Hu, H. Wu, T. Zhu, C. Fu, J. He, P. Ying and X. Zhao, Adv. Energy Mater., 2015, 5, 1500411.
- 23 R. Kim and M. S. Lundstrom, J. Appl. Phys., 2012, 111, 024508.
- 24 J.-H. Bahk and A. Shakouri, Appl. Phys. Lett., 2014, 105, 052106.
- 25 R. Kim and M. S. Lundstrom, J. Appl. Phys., 2011, 110, 034511.
- 26 S. Sadasivam, U. V. Waghmare and T. S. Fisher, J. Appl. Phys., 2015, 117, 134502.
- 27 M. Thesberg, H. Kosina and N. Neophytou, J. Appl. Phys., 2016, 120, 234302.
- 28 Y. Ouyang, Y. Xie, Z. Zhang, Q. Peng and Y. Chen, J. Appl. Phys., 2016, 120, 235109.
- 29 S. Wang, H. Li, R. Lu, G. Zheng and X. Tang, Nanotechnology, 2013, 24, 285702.
- 30 S. Li, R. Wang, W. Zhu, M. Chu, Z. Huang, Y. Zhang, W. Zhao, F. Liu, J. Luo, Y. Xiao and F. Pan, Adv. Electron. Mater., 2020, 6, 2000292.
- 31 S. Li, T. Fan, X. Liu, F. Liu, H. Meng, Y. Liu and F. Pan, ACS Appl. Mater. Interfaces, 2017, 9, 3677-3685.
- 32 J. Amrit, J. Phys. D: Appl. Phys., 2006, 39, 4472-4477.
- 33 J.-H. Bahk and A. Shakouri, Appl. Phys. Lett., 2014, 105, 052106.